

# TurboGAN: An Adversarial Learning Approach to Spatially-Varying Multiframe Blind Deconvolution with Applications to Imaging Through Turbulence

Brandon Y. Feng\*, Mingyang Xie\*, Christopher A. Metzler

**Abstract**—We present a self-supervised and self-calibrating multi-shot approach to imaging through atmospheric turbulence, called TurboGAN. Our approach requires no paired training data, adapts itself to the distribution of the turbulence, leverages domain-specific data priors, outperforms existing approaches, and can generalize from tens to tens of thousands of measurements. We achieve such functionality through an adversarial sensing framework adapted from CryoGAN [1], which uses a discriminator network to match the distributions of captured and simulated measurements. Our framework builds on CryoGAN by (1) generalizing the forward measurement model to incorporate physically accurate and computationally efficient models for light propagation through anisoplanatic turbulence, (2) enabling adaptation to slightly misspecified forward models, and (3) leveraging domain-specific prior knowledge using pretrained generative networks, when available. We validate TurboGAN in simulation using realistic models for atmospheric turbulence-induced distortion.

**Index Terms**—Adversarial training, multiframe blind deconvolution, atmospheric turbulence.

## I. INTRODUCTION

Atmospheric turbulence causes long-range imaging systems to capture blurry and distorted measurements. These distortions are caused by the heterogeneous refractive index of the atmosphere: When light propagates through the atmosphere, the heterogeneity will delay the phase of the wavefront, and this delay determines the optical system’s point spread function (PSF). When the heterogeneity is distributed over a volume the turbulence is said to be anisoplanatic and the PSF is spatially variant. Accordingly, imaging through anisoplanatic turbulence can be described by the equation

$$\mathbf{y}_i(u, v) = \mathbf{h}_i(u, v) * \mathbf{x} + \boldsymbol{\epsilon}_i, \quad (1)$$

where  $(u, v)$  are pixel coordinates,  $\mathbf{y}_i \in \mathbb{R}^{N \times N}$  is an observed blurry image,  $\mathbf{h}_i(u, v) \in \mathbb{R}^{M \times M}$  is a spatially-varying blur kernel at location  $(u, v)$ ,  $\mathbf{x} \in \mathbb{R}^{N \times N}$  is the target being imaged,  $\boldsymbol{\epsilon}_i \in \mathbb{R}^{N \times N}$  is (possibly signal dependent) noise,  $N$  is the image size in pixels, and  $M$  is the kernel size in pixels. When imaging a stationary target through dynamic turbulence, the signal  $\mathbf{x}$  is fixed while at each time step the measurements  $\mathbf{y}_1, \mathbf{y}_2, \dots, \mathbf{y}_L$  experience different blur kernels  $\mathbf{h}_1, \mathbf{h}_2, \dots, \mathbf{h}_L$ .

The central challenge posed by the forward model described by Equation (1) is that the underlying turbulence is *stochastic*

across different locations and instances of time. Without prior information or measurements such as a guidestar [2], the spatially-varying blur kernels  $\{\mathbf{h}_i\}_{i=1}^L$  are unknown and recovering  $\mathbf{x}$  requires solving a spatially-varying multiframe blind deconvolution problem.

### A. Contributions

We develop a new self-supervised spatially-varying multiframe blind deconvolution algorithm for imaging through atmospheric turbulence. The proposed algorithm uses an adversarial sensing framework shown in Figure 1, in which a neural representation of a scene and a physically accurate differentiable forward model are combined to generate synthetic measurements. A discriminator network is then used to compare the *distributions* of the synthesized and experimental measurements to provide a feedback signal that improves the quality of the neural scene representation. Adversarial sensing is explained in detail in Section III.

To our knowledge, this is the first application of adversarial sensing, which was first developed for unknown-view-tomography in the context of single-particle cryogenic electron microscopy (cryo-EM) [1], to multiframe blind deconvolution or imaging through atmospheric turbulence. Adversarial sensing provides several distinct advantages over previous methods. Unlike classical algorithms, our method requires neither reconstructing nor marginalizing over the latent variables which characterize the turbulence associated with each measurement. Unlike supervised deep learning methods, our method does not rely on a large corpus of training data and is thus robust to out-of-distribution test data/turbulence-strengths. Moreover, while many (but not all [3]) supervised deep learning methods make predictions based on a fixed numbers of input frames in a single-shot fashion, our method is able to iteratively refine its prediction given an arbitrary number of measurements.

Our largest contributions can be summarized as follows.

- 1) We develop a novel adversarial sensing framework for multiframe imaging through anisoplanatic turbulence.
- 2) We demonstrate adversarial sensing can be combined with off-the-shelf generative networks (StyleGAN2 [4]) to impose strong but specialized priors on the reconstructed images.
- 3) We demonstrate adversarial sensing can be combined with untrained generative networks (DIP [5]) to impose weak but flexible priors on the reconstructed images.

The authors are with the Department of Computer Science, University of Maryland, College Park, MD, 20742, USA (e-mail: yfeng97@umd.edu; mingyang@umd.edu; metzler@umd.edu). This work was supported in part by the AFOSR Young Investigator Program.

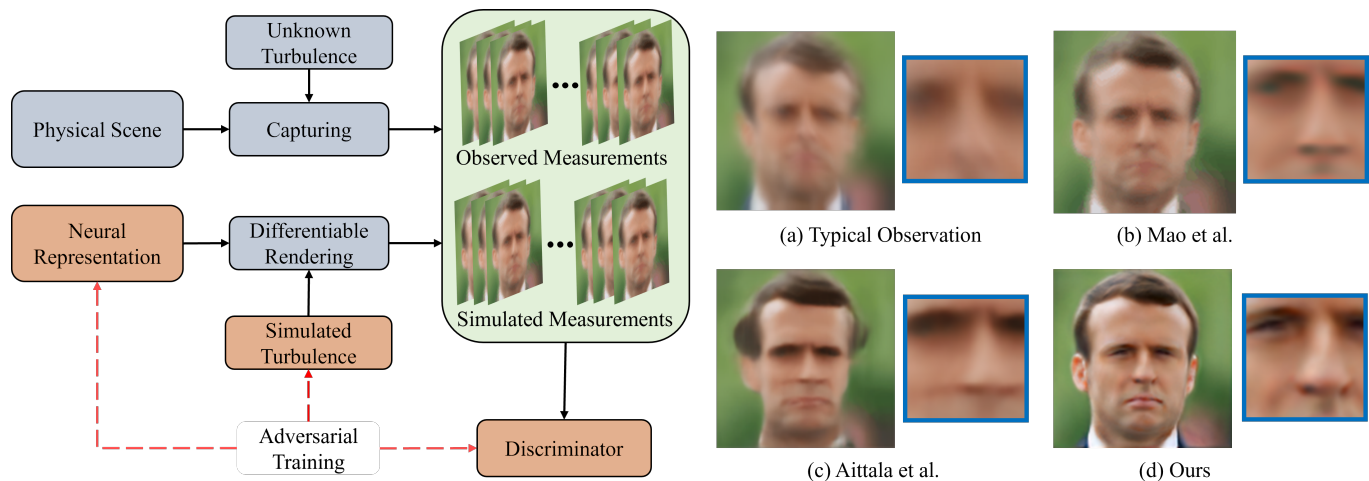


Fig. 1. **TurbuGAN Framework and Experimental Reconstructions.** Capturing images through turbulence often leads to highly distorted and blurry observations, like (a). The TurbuGAN framework (left) can use a collection of distorted measurements and produce reconstructions, like (d), that are sharper and contain fewer artifacts than those produced by existing methods, like (b) and (c). TurbuGAN achieves this using adversarial sensing: A neural representation of the scene is fed into a physically accurate and differentiable rendering engine that models the effects of atmospheric turbulence to produce simulated measurements. A discriminator compares the distribution of these measurements with the distribution of true observations of the scene. The feedback the discriminator provides is used to update the neural representation and thereby reconstruct the scene.

- 4) We extend adversarial sensing to deal with misspecified forward model and show that this extension allows us to adapt to unknown turbulence conditions.
- 5) We validate our method on challenging simulated dataset and demonstrate exceptional performance.

### B. Limitations

While our work represents a fundamentally new approach to imaging through turbulence, it does come with a few notable limitations. First, our current work assumes we have multiple measurements of a static object and does not currently support dynamic scenes. Second, while the forward model used in this paper has been experimentally validated [6], our current results are simulation-only. Finally, our method is very computationally expensive: reconstructing a single  $128 \times 128$  image from 2,000 distorted observations takes around five hours on a high-end GPU.

## II. RELATED WORK

### A. Imaging Through Turbulence

Over the last 30 years, many multiframe blind deconvolution and turbulence-removal algorithms have been developed.

The oldest and most widely used approach to multiframe imaging through turbulence is lucky imaging. Lucky imaging is founded on the concept that even under moderately severe turbulence conditions, given a large number of measurements there is high probability that at least one measurement will experience very little turbulence-induced distortion [8]. Based on this insight, lucky imaging techniques extract and fuse the “lucky” frames from an image sequence by identifying the frames that maximize some quality metric; often sharpness [9]. Extracting the lucky patches from an image sequence is often an important step during the registration process used with modern anisoplanatic turbulence removal algorithms as

well [7]. As one might expect, lucky imaging provides limited benefits when all the measurements are blurry and there are no lucky frames to take advantage of.

When all the images in the sequence are blurry, one needs to perform deconvolution as well. Expectation-maximization (EM) based deconvolution algorithms reconstruct the image while marginalizing over the distribution of the blur kernels [10]. However, the computation cost of EM-based methods scales exponentially with the number of latent variables, making it impractical to deploy in applications involving high-dimensional continuous latent variables (i.e., high-resolution spatially varying blur kernels).

A simpler alternative to EM is alternating minimization (AM). AM-based deconvolution algorithms attempt to reconstruct both the blur kernels and the image by imposing various priors on each. For instance, in [11] the authors impose a sparse total variation prior on the image and a sparse and positive constraint on the blur kernels. Recent efforts have imposed more accurate models on the images (non-local self-similarity [12]) and the blur kernels (Kolmogorov turbulence) [7]. To our knowledge, the method developed in [7] represents the current state-of-the-art in multiframe imaging through turbulence.

Deep learning provides the possibility to develop turbulence removal algorithms that benefit from a large amount of training data. Several recent works have trained deep neural networks to remove atmospheric distortions from a single image [13]–[15]. Recently, Mao et al. [6] trained a convolutional neural network to reconstruct a sharp image from 50 frames degraded by atmospheric turbulence. Their method achieved performance only incrementally worse than state-of-the-art classical methods while running significantly faster. For more traditional blind deconvolution tasks, like removing camera shake, researchers have developed methods [3], [16] that generalize across an arbitrary number of frames. All these

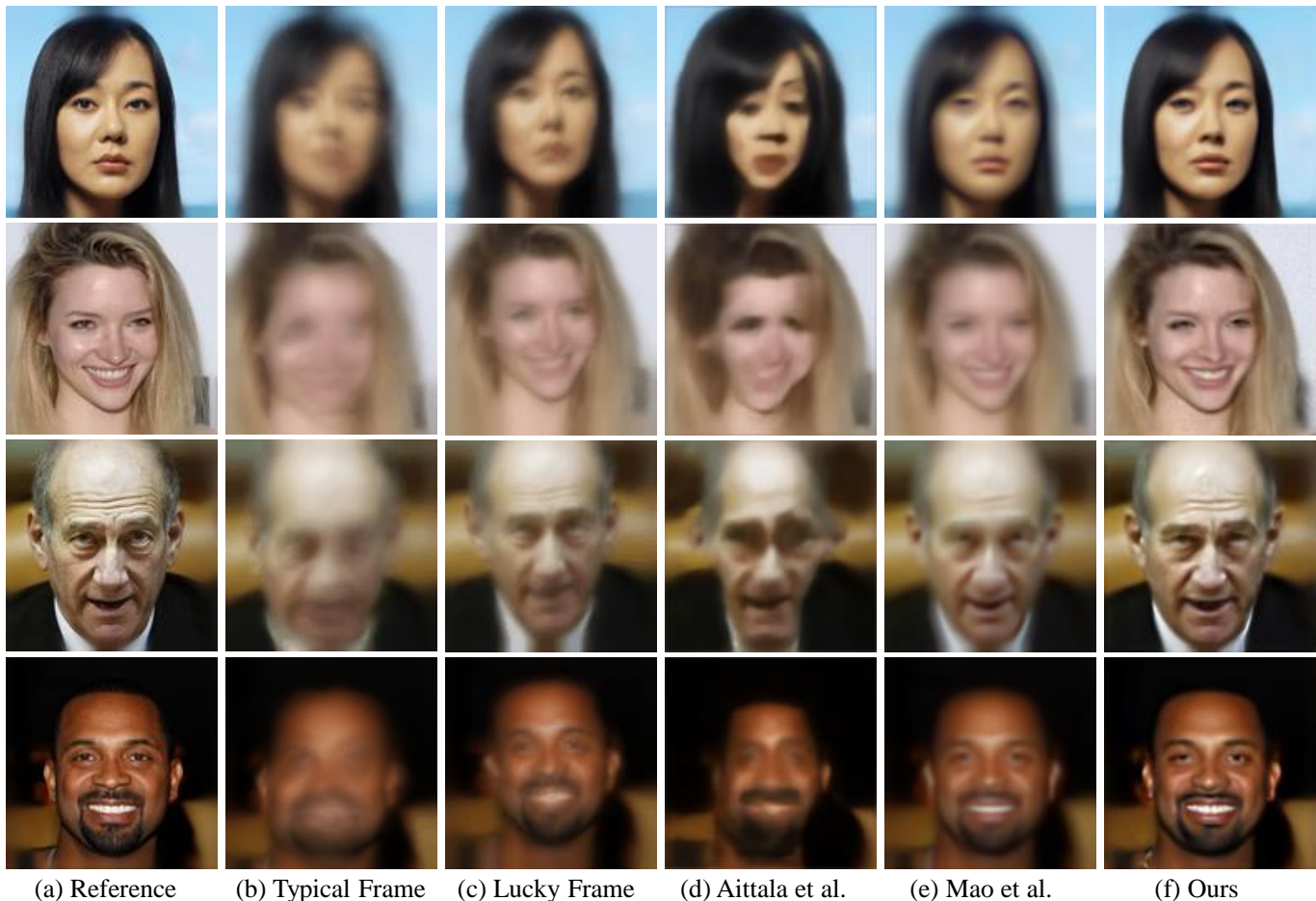


Fig. 2. **Reconstructing Sharp Images from Blurry Measurements.** Given the reference images (a), we simulate 2000 observations distorted by spatially-varying turbulence. Typical distorted frames are shown in (b) and handpicked lucky frames are shown in (c). The results produced by [3] are shown in (d); they contain significant warping artifacts. The results produced by [7] are shown in (e); they avoid warping artifacts but are not much sharper than the lucky frames. Our method (f) produces sharp reconstructions whose fine details and structure are consistent with the reference images.

methods train their network to a specific blur kernel family or turbulence level, limiting their adaptability.

### B. Imaging Inverse Problem with Generative Networks

By constraining reconstructed images to lie within the range of a deep generative network and then finding the latent parameters consistent with the measurements, several research groups have solved under-determined imaging inverse problems such as compressive sensing [17]–[22] and phase retrieval [23]–[25]. As shown in [5], this framework can be effective even if the generative network is untrained.

By estimating both the object and unknown forward model, this framework can be adapted to problems with unknown forward models, such as blind demodulation [26], blind deconvolution [27], [28], and blind super-resolution [29]. However, such approaches do not easily apply to our multiframe anisoplanatic turbulence removal problem because they would require reconstructing all the blur kernels associated with all the pixels of all the observations.

### C. CryoGAN

CryoGAN [1] similarly reconstructs images by fitting a network to a collection of measurements, but it does so using a fundamentally different approach which compares the *distributions* of predicted and real observations. We refer to this approach as adversarial sensing.

In CryoGAN, adversarial sensing compares the distributions of simulated and captured tomographic projections and updates the reconstruction to make the two distributions more alike. Adversarial sensing allows one to fit a network to the observations even when one-to-one correspondence between an observation and its associated latent variables cannot be established. In the context of cryo-EM, this challenge arises because the latent orientation associated with each observed projection of the underlying 3D object (molecule) is highly under-determined. In this work, we extend adversarial sensing to the task of turbulence removal.

## III. METHODS: ADVERSARIAL SENSING

Our goal is to recover the underlying target scene  $\mathbf{x}$  given a set of observations  $\{\mathbf{y}_i\}_{i=1}^L$ , characterized by the equation

$$\mathbf{y}_i(u, v) = \mathbf{h}_i(u, v) * \mathbf{x} + \epsilon_i, \quad (2)$$

where the set of spatially-varying blur kernels  $\{\mathbf{h}_i\}_{i=1}^L$  are unknown. We approach this challenging blind deconvolution problem with adversarial sensing.

The adversarial sensing reconstruction pipeline is illustrated in Figure 1. In our framework, a neural scene representation (e.g., the output of a generator network) serves as our reconstruction of the distortion-free scene. This reconstruction is fed to a physics-based differentiable forward model which synthesizes distorted measurements. These synthesized measurements are fed into a discriminator network which is trained to differentiate between these synthetic measurements and the true observations. In effect, the discriminator provides a feedback signal about whether the synthesized data’s distribution,  $p_{h*\tilde{\mathbf{x}}}(\mathbf{y})$ , is equal to the true data’s distribution,  $p_{h*x}(\mathbf{y})$ . This feedback signal is used to adapt the reconstruction (and potentially the forward model as well) until  $p_{h*\tilde{\mathbf{x}}}(\mathbf{y})$  and  $p_{h*x}(\mathbf{y})$  are indistinguishable. In doing so, we reconstruct the scene  $\mathbf{x}$ .

### A. Theoretical Justification

Before providing the details of each stage of adversarial sensing, we demonstrate that in the much simpler case of isoplanatic turbulence (spatially-invariant blur), matching the distributions of the simulated and observed noise-free measurements reconstructs the scene to some degree.

**Theorem III.1.** *Let  $p_{h*x}(\mathbf{y})$  denote the distribution associated with noiseless spatially-invariant measurements*

$$\mathbf{y} = \mathbf{h} * \mathbf{x}, \text{ where } \mathbf{h} \sim p_h. \quad (3)$$

*Let  $p_{h*\tilde{\mathbf{x}}}(\mathbf{y})$  denote the distribution associated with measurements formed by a reconstruction  $\tilde{\mathbf{x}}$  and blur kernels following  $p_h$ . Then,*

$$p_{h*x}(\mathbf{y}) = p_{h*\tilde{\mathbf{x}}}(\mathbf{y}) \implies \mathbf{G} \circ |\mathcal{F}\mathbf{x}| = \mathbf{G} \circ |\mathcal{F}\tilde{\mathbf{x}}|, \quad (4)$$

where  $\circ$  denotes a Hadamard (elementwise) product,  $\mathcal{F}$  denotes the 2D Fourier transform, and  $\mathbf{G} = \mathbb{1}_+(\mathbb{E}[|\mathcal{F}\mathbf{h}|^2])$  where  $\mathbb{1}_+(\cdot)$  denotes an indicator function that is 1 if its argument is greater than 0.

In effect, Theorem III.1 states that if adversarial sensing can match the distributions of the observed and simulated measurements, it will reconstruct  $\mathbf{x}$  accurately up to the invariances (e.g., translation) associated with the masked phase retrieval problem defined by the right hand side of Equation (4). A proof can be found in Appendix A.

### B. Neural Representation

Instead of directly reconstructing  $\mathbf{x} \in \mathbb{R}^{N \times N}$ , we optimize the weights  $\boldsymbol{\theta}$  of a convolutional network  $\mathcal{G}_{\boldsymbol{\theta}}$  where  $x = \mathcal{G}_{\boldsymbol{\theta}}(z)$ . As explained in Section III-D, during training,  $z$  is fixed after initialization while a discriminator provides the gradients used to update  $\boldsymbol{\theta}$ . The specific initialization scheme of  $z$  varies based on the level of knowledge we have about the target scene, and is discussed in detail in Section IV.

### C. Physically Accurate Differentiable Forward Model for Anisoplanatic Atmospheric Turbulence

Adversarial sensing relies upon having access to a physically accurate forward model that can produce synthetic measurements that follow the same distribution as real measurements. This forward model also needs to be differentiable, so that one can back-propagate through it and update the neural representation of the scene.

As explained in [30], the blur kernel  $\mathbf{h}$  associated with the turbulence at location  $(u, v)$  is related to the phase errors  $\phi(u, v)$  at that location via the expression

$$\mathbf{h}(u, v) = |\mathcal{F}(e^{-j\phi(u, v)})|^2. \quad (5)$$

Thus, one can generate realistic blur kernels by generating realistic phase errors  $\phi(u, v)$  for all  $(u, v)$ .

At each pixel location  $(u, v)$  one can approximate  $\phi(u, v)$  with the first  $M$  Zernike polynomials as

$$\phi(u, v) = \sum_{i=1}^M \alpha_i Z_i(u, v), \quad (6)$$

where  $Z_i$  is the  $i^{\text{th}}$  Zernike basis and  $\alpha_i$  is its corresponding coefficient [31]. The vector of coefficients  $\boldsymbol{\alpha}$  follows a zero-mean normal distribution with covariance matrix  $\boldsymbol{\Sigma}$ . Detailed derivations [31], [32] show that  $\boldsymbol{\Sigma}$  depends on the ratio of the imaging system’s aperture’s diameter  $D$  and the Fried parameter  $r_0$  [8], which characterizes the turbulence strength.

The correlations between the Zernike phase errors at adjacent locations are similarly well understood. Thus, to model propagation through atmospheric turbulence one can (1) sample a collection of correlated Zernike coefficients for every pixel in an image, (2) use equations (5) and (6) to compute the PSF associated with each pixel in the image, and (3) convolve every pixel in the scene with its associated PSF [32]. As one might expect, performing these computations explicitly is extremely computationally expensive.

Fortunately, the recently proposed phase-to-space (P2S) transform [6] bypasses the computationally expensive blur kernel generation process (equations (5) and (6)) by training a neural network to learn a mapping directly between the Zernike coefficients and blur kernels. Simulation results demonstrate that the blur kernels generated with the P2S transform are physically accurate, consistent with existing theory, and can be evaluated 300–1000 $\times$  faster than previous physics-based forward models [6]. Accordingly, in this work the P2S transform both generates the ground truth observations and serves as our differentiable rendering engine which is used to generate the synthetic measurements in the adversarial sensing pipeline.

### D. Optimization Objectives

Adversarial sensing follows the standard adversarial learning paradigm, where one trains a generator  $\mathcal{G}$  to trick a discriminator  $\mathcal{D}$  and also trains  $\mathcal{D}$  not to get tricked. The key difference between adversarial sensing and conventional GAN training lies in the fact that the generation and discrimination take place on distorted measurements, rather than the distortion-free scene that produced them.

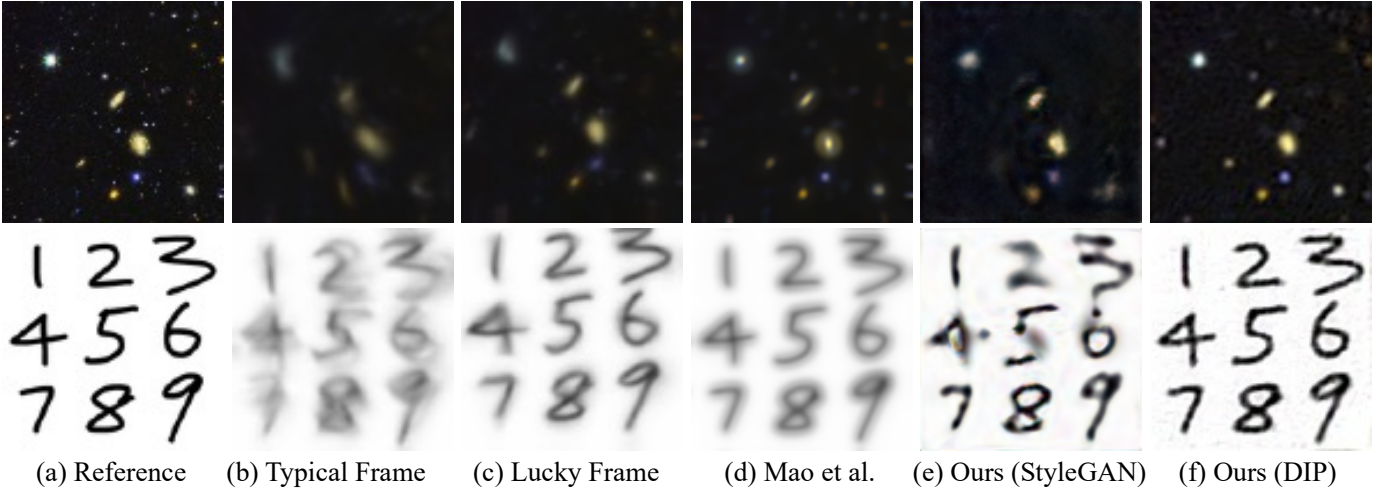


Fig. 3. **Turbulence Removal on Non-face Targets.** We extend our experiments to non-face targets such as images of stars and hand-written digits. The reference target images, typical frames, and lucky frames and shown in (a), (b), and (c), respectively. The results produced by [7] are shown in (d); there are few artifacts but the reconstructions are somewhat blurry. When we initialize the generator with the pretrained StyleGAN2 weights, the results (e) suffer from visible artifacts – these images are very unlike the faces StyleGAN2 was trained with. However, when using a randomly initialized generator (similar to DIP), the reconstructions (f) contain minimal artifacts and are much sharper than the other methods. These results demonstrate that our framework extends beyond face data and generalize well on situations where a pretrained prior (like StyleGAN2 weights for face data) is not easily available.

1) *Optimizing The Discriminator:* To train the discriminator, for each training batch we first gather a collection of  $K$  observed distorted measurements  $\mathbf{y}$ . Next, we obtain the current estimated target image  $\mathcal{G}(z) = \hat{\mathbf{x}}$  and construct fake observations  $\{\hat{\mathbf{y}}_i(u, v) = \hat{\mathbf{h}}_i(u, v) * \hat{\mathbf{x}}\}$ .

We then send both  $\{\hat{\mathbf{y}}_i\}$  and  $\{\mathbf{y}_i\}$  to the discriminator to compute  $\{D(\mathbf{y}_i)\}$  and  $\{D(\hat{\mathbf{y}}_i)\}$ . Finally, we update the discriminator  $D$  with loss function  $L_D = L_D^{real} + L_D^{fake} + L_D^{mix}$ , where the three terms are defined as:

$$L_D^{real} = \frac{p_d}{K} \sum_{i=1}^K D(\mathbf{y}_i)^2 - \frac{1}{K} \sum_{i=1}^K D(\mathbf{y}_i), \quad (7)$$

$$L_D^{fake} = \frac{1}{K} \sum_{i=1}^K D(\hat{\mathbf{y}}_i). \quad (8)$$

$$L_D^{mix} = \frac{p_r}{K} \sum_{i=1}^K (\|\nabla_{\mathbf{b}} D(\mathbf{b})\|_2 - 1)^2 \quad (9)$$

This loss function is based on the Wasserstein GAN loss [33], and  $p_d$  and  $p_r$  are both regulatory parameters. In the third term  $L_D^{mix}$ ,  $\mathbf{b} = \alpha \hat{\mathbf{y}}_i + (1 - \alpha) \mathbf{y}_i$ , where  $\alpha$  are randomly sampled from  $[0, 1]$ . This loss term softly enforces the Lipschitz constraint on the discriminator and thus decreases training difficulty.

2) *Optimizing The Generator:* Optimizing the generator is straightforward. We encourage the generator to produce fake samples that are scored higher by the discriminator. The generator’s loss is defined as:

$$L_G = -\frac{1}{K} \sum_{i=1}^K D(\hat{\mathbf{y}}_i). \quad (10)$$

## IV. EXPERIMENTS

In this section, we perform several experiments to evaluate the proposed method on the turbulence removal problem. We also analyze how varying different attributes of the problem setting affect its performance. Unless otherwise noted, in all experiments we simulate  $L = 2,000$  measurements for each scene with an aperture diameter  $D$  of 0.1 meter, a Fried parameter  $r_0$  of 0.05, and a distance to target of 1000 meters. In each iteration, we use a batch size  $K = 32$  for both observed and simulated measurements. All target images have a resolution of  $128 \times 128$ . Both  $D$  and  $\mathcal{G}$  are trained using the Adam optimizer [34]; we first warm up  $D$  for 5000 iterations while fixing  $\mathcal{G}$ ; afterwards, we alternate between updating  $D$  for six iterations and  $\mathcal{G}$  for one iteration. Training stops after 100,000 iterations and takes about five hours on an NVIDIA RTX A6000 GPU. Our framework is implemented in PyTorch [35] and will be released upon acceptance.

### A. Face Images

We first simulate turbulence distorted images of 4 real human faces from the CelebA dataset [36] with diverse facial attributes, age, ethnicity, and gender. We apply the fast simulator introduced by Mao et al. [6] to generate realistic anisoplanatic turbulence.

While our neural representation  $\mathcal{G}_\theta$  is architecture-agnostic in concept, since we only focus on face data in the current experiments, we take full advantage of the prior knowledge of StyleGAN2 and use its network architecture with weights pretrained on the FFHQ dataset [37].

During training, we first optimize the input vector  $z$  similar to the first stage of the Pivotal Tuning Inversion (PIT) approach [38], which has demonstrated state-of-the-art performance on GAN inversion. Specifically, we optimize  $z$  such that the initial generator output matches the reconstructed result

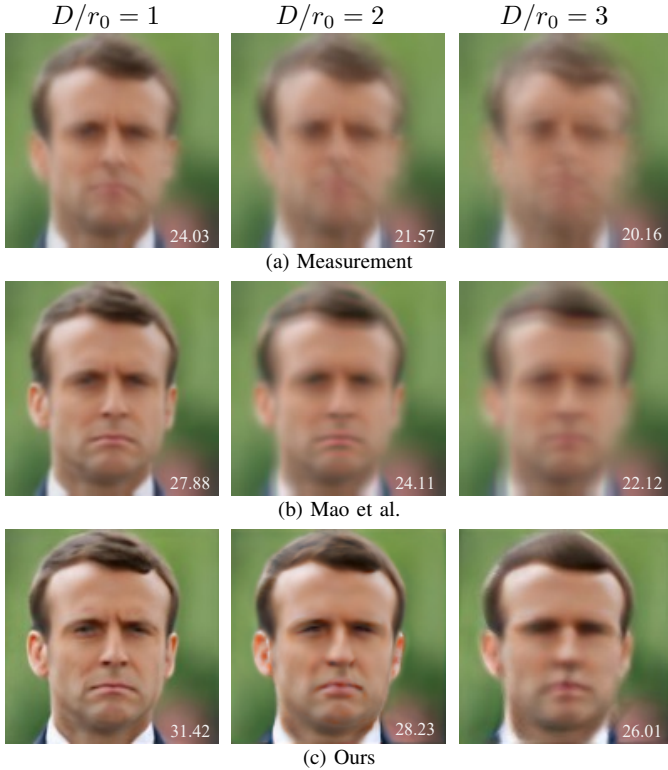


Fig. 4. **Effect of Varying the Turbulence Strength  $D/r_0$ .** We compare the visual quality of a sample measurement (top row), the reconstruction by [7] (middle row), and by our method (bottom row) at 3 different  $D/r_0$  levels from left to right. Our method outperforms [7] at all 3 turbulence strengths by producing sharper and more accurate reconstructions.

of [7]. We then optimize the network weights based on the training objective described in Section III-D.

We perform experiments to compare TurbuGAN with two other deblurring algorithms introduced in [7] and [3]. Qualitative comparisons are presented in Figure 2. TurbuGAN clearly succeeds in restoring the original image, while the baseline methods produce blurry images with obvious artifacts.

Figure 4 demonstrates that TurbuGAN consistently outperforms [7] across a variety turbulence levels.

### B. Non-face Images Without Generator Prior

While previous results in Figure 2 demonstrate that TurbuGAN significantly improves the turbulence removal quality on face data, they do not answer whether it generalizes well on other data domains where we cannot initialize  $\mathcal{G}$  with pretrained weights that offer a good prior like StyleGAN2. In this section, we extend our framework to non-face data such as images of stars and handwritten digits. Instead of using the StyleGAN2 network, we use a U-Net architecture [39] for the generator and randomly initialize its weights. This setup is similar to the well-known Deep Image Prior (DIP) [5] method. We first initialize the generator’s output to be the mean of the distorted measurements, and then proceed to the training pipeline described in Section III-D.

The results in Figure 3 clearly demonstrate that our method extends to data domains where we cannot initialize the generator with domain-specific prior knowledge.

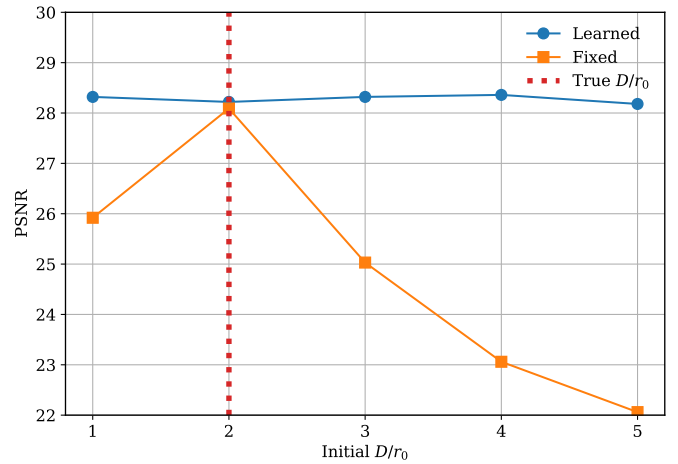


Fig. 5. **Adapting to Mismatched Turbulence Strength  $D/r_0$ .** We set the true unknown turbulence strength level  $D/r_0$  equal to 2 (red vertical line). We initialize our framework with different  $D/r_0$  levels ranging from 1 to 5, and we compare the performance (PSNR) between learning and fixing the initial  $D/r_0$ . The orange curve shows that the reconstruction quality significantly deteriorates when the framework sticks to a misspecified turbulence strength level. The blue curve shows that by updating  $D/r_0$  during training, our method is able to overcome severe initial mismatches and achieve almost the same performance as when it is correctly initialized with  $D/r_0 = 2$ .

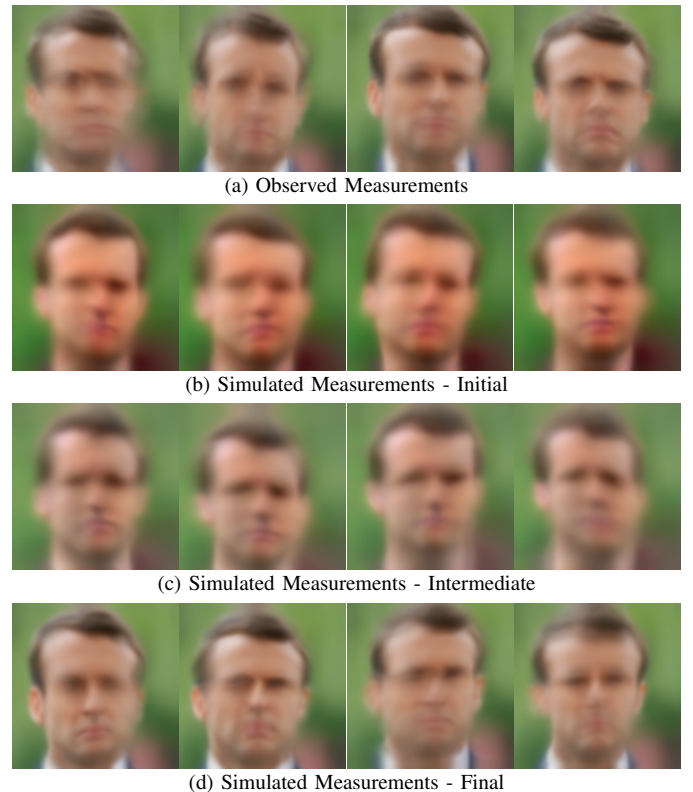


Fig. 6. **Comparison Between the Distribution of Observed and Simulated Measurements.** We show randomly selected frames from the observed measurements (a), simulated measurements at network initialization (b), simulated measurements at an intermediate iteration (c), and simulated measurements at the final iteration (d). The distribution of the simulated measurements (b)-(d) become increasingly similar to the distribution of the observed measurements (a) over time.

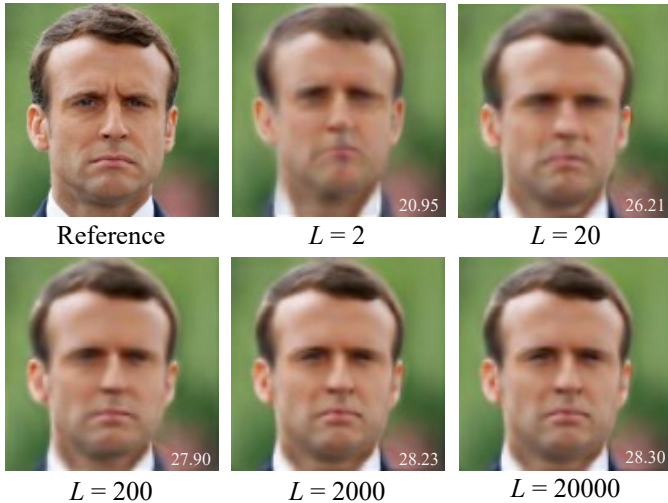


Fig. 7. **Effect of Varying the Number of Measurements  $L$ .** We deploy our method to remove turbulence in face images using different number of measurements  $L$  under turbulence strength  $D/r_0 = 2$ . We measure the reconstruction quality (in PSNR) against the reference and display it on the bottom right. The reconstruction quality gradually improves as  $L$  increases, showing our framework benefits from having access to more observations.

### C. Adapting to Misspecified Forward Models

In our differentiable turbulence simulator [6], the turbulence strength is described by  $D/r_0$ , where  $D$  is the aperture diameter and  $r_0$  is the Fried parameter [8]. In previous experiments, we set the same  $D/r_0$  values when we generate observed and simulated measurements. However, while in real-world imaging scenarios the aperture diameter  $D$  is usually known, the Fried parameter  $r_0$  is likely unknown. Our framework would have limited use if it required knowing the precise turbulence strength  $D/r_0$  of the scene.

In this section, we demonstrate our framework’s can be made robust to misspecified forward models by treating  $D/r_0$  as a learnable parameter. To analyze the impact of learning to update  $D/r_0$  in the simulator, we initialize the simulator with various  $D/r_0$  values and then compare the final performance when one learns or fixes the  $D/r_0$  parameter. In this set of experiments, we select the same face image as the target and set the true unknown  $D/r_0 = 2$  and test under five conditions with different initial  $D/r_0$  ranging from 1 to 5.

In Figure 5, we plot the final reconstruction quality (measured in PSNR) against different misspecified initial  $D/r_0$ . Evidently, learning to adjust the turbulence strength level  $D/r_0$  during training overcomes the incorrect initialization and significantly improves the reconstruction quality.

## V. ANALYSIS AND DISCUSSION

### A. Distribution Matching

As noted in Section III-A, TurbuGAN’s reconstruction capabilities hinge on its ability to successfully match the observed and simulated distributions. In Figure 6, we demonstrate that during adversarial training, the distribution of the simulation measurements gradually becomes indistinguishable from the true measurements’ distribution.

### B. Measurement Usage

Among learning-base methods, TurbuGAN is somewhat unique in its ability to take advantage of an arbitrary number of measurements. As demonstrated in Figure 7, TurbuGAN’s reconstruction quality increases with the number of available measurements. While our method can produce reasonable reconstructions using only 20 measurements, the more it has the better it does.

### C. Connection to Expectation Maximization

Although the well-known EM algorithm can be also regarded as comparing the distributions of real and simulated measurements, in EM this comparison is performed explicitly using analytic expressions, rather than implicitly with a discriminator. Accordingly, EM requires one to discretize the distribution of the latent variables (in order to make marginalization computationally feasible). EM also requires analytically maximizing the log likelihood of measurements. This requirement often results in a Gaussian assumption on the noise, which turns the log-likelihood maximization problem into a easy-to-solve least squares problem.

Unfortunately, EM does not scale to high dimensional latent variables. For example, even with 15 Zernike coefficients each discretized into only 5 bins, each E step of the EM algorithm would require computing  $5^{15}$  potential measurements per image! Modeling anisoplanatic turbulence is significantly harder still.

Our method avoids the high computational complexity associated with the EM algorithm and is able to reconstruct the underlying target without explicitly solving for the continuous latent variables associated with each measurement.

## VI. CONCLUSION

This work introduces TurbuGAN, a spatially-varying multiframe blind deconvolution method based on the adversarial sensing concept first proposed in CryoGAN [1]. TurbuGAN is able to effectively synthesize thousands of highly distorted images, each modeling the effects of severe atmospheric turbulence, into a single high-fidelity reconstruction of a scene. While TurbuGAN’s performance is especially strong in domains where it has access to prior information (via a pretrained generative network), when combined with untrained networks, TurbuGAN is also surprisingly effective in domains where no such priors are available. Moreover, TurbuGAN can adapt to misspecified forward models.

Adversarial-sensing-based reconstruction methods, like TurbuGAN, represent a fundamentally new approach to solving inverse problems in imaging. They open up the possibility of applying deep learning to tackle previously unsolvable inverse problems in imaging where limited or no training data is available and only the distribution of the forward measurement model is known.

### APPENDIX A PROOF OF THEOREM III.1

The following provides a proof for Theorem III.1, which states that by matching the distributions of the observed and

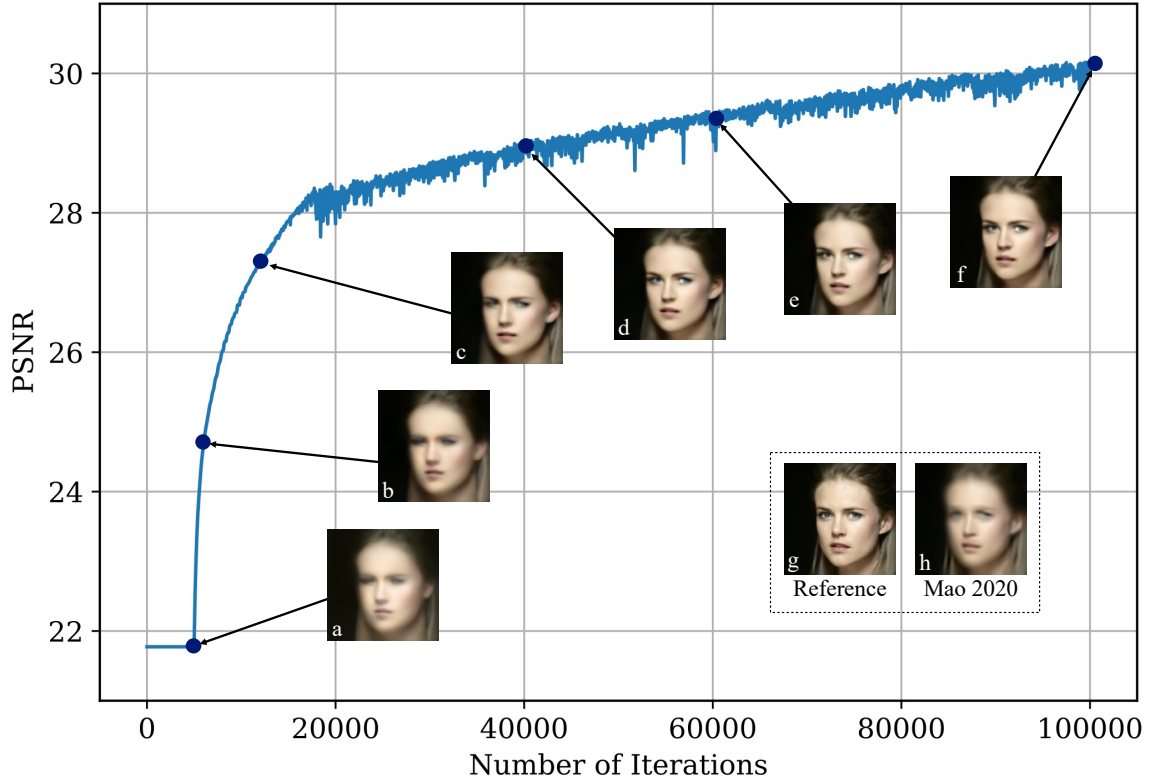


Fig. 8. **Reconstruction Evolves During Training.** For an experiment with the same settings as in Figure 2, we plot the PSNR values against the number of iterations. We also present the initial generator output (a), the intermediate reconstructions (b-e), and the final reconstruction (f), along with their corresponding spot in the PSNR curve. The reference target image (g) and the reconstruction by [7] (h) are placed at the lower right corner for comparison. Both the visual quality and PSNR steadily improve over time.

simulated measurements, adversarial sensing will reconstruct the Fourier magnitude of  $\mathbf{x}$  accurately at all frequencies where the power spectral density of the blur kernels is non-zero.

*Proof.* If two random vectors have the same distribution, then their Fourier transforms will have the same distribution. Thus, if

$$p_{h \star x}(\mathbf{y}) = p_{h \star \tilde{x}}(\mathbf{y}), \quad (11)$$

then

$$p_{H \circ X}(\mathbf{Y}) = p_{H \circ \tilde{X}}(\mathbf{Y}), \quad (12)$$

where  $\mathbf{H}$ ,  $\mathbf{X}$ ,  $\tilde{\mathbf{X}}$ , and  $\mathbf{Y}$  denote the Fourier transforms of  $\mathbf{h}$ ,  $\mathbf{x}$ ,  $\tilde{\mathbf{x}}$ , and  $\mathbf{y}$  respectively. (Recall that convolution in the spatial domain is equivalent to elementwise multiplication in the spatial frequency domain.)

Random variables with the same distributions have the same moments, therefore we have that

$$\mathbb{E}[|\mathbf{H} \circ \mathbf{X}|^2] = \mathbb{E}[|\mathbf{H} \circ \tilde{\mathbf{X}}|^2]. \quad (13)$$

This implies

$$\mathbf{X}^2 \circ \mathbb{E}[|\mathbf{H}|^2] = \tilde{\mathbf{X}}^2 \circ \mathbb{E}[|\mathbf{H}|^2]. \quad (14)$$

Equation (14) implies

$$\mathbf{X}^2(K_u, K_v) = \tilde{\mathbf{X}}^2(K_u, K_v) \quad \forall (K_u, K_v) \quad (15)$$

$$\text{s.t. } \mathbb{E}[|\mathbf{H}|^2](K_u, K_v) \neq 0. \quad (16)$$

Let  $\mathbf{G}$  denote a frequency domain mask with entries equal to 0 at spatial frequencies  $(K_u, K_v)$  where the power spectral density of  $\mathbf{h}$  is 0, and with entries equal to 1 everywhere else. That is,

$$\mathbf{G}(K_u, K_v) = \begin{cases} 1, & \text{if } \mathbb{E}[|\mathbf{H}|^2](K_u, K_v) > 0, \\ 0, & \text{otherwise.} \end{cases} \quad (17)$$

We can now concisely represent condition (15) with the expression

$$\mathbf{G} \circ \mathbf{X}^2 = \mathbf{G} \circ \tilde{\mathbf{X}}^2, \quad (18)$$

which implies

$$\mathbf{G} \circ |\mathbf{X}| = \mathbf{G} \circ |\tilde{\mathbf{X}}|. \quad (19)$$

□

## APPENDIX B CONVERGENCE

Figure 8 highlights how the neural representation of the scene changes over time. We do not use early stopping since we consistently observe that as the number of iterations increases, the reconstruction quality steadily improves in terms of both visual quality and quantitative metrics such as PSNR.

## REFERENCES

- [1] H. Gupta, M. T. McCann, L. Donati, and M. Unser, "CryoGAN: A New Reconstruction Paradigm for Single-Particle Cryo-EM Via Deep Adversarial Learning," *IEEE Transactions on Computational Imaging*, vol. 7, pp. 759–774, 2021.
- [2] J. M. Beckers, "Adaptive Optics for Astronomy: Principles, Performance, and Applications," *Annual Review of Astronomy and Astrophysics*, vol. 31, no. 1, pp. 13–62, 1993.
- [3] M. Aittala and F. Durand, "Burst Image Deblurring Using Permutation Invariant Convolutional Neural Networks," in *Proceedings of the European Conference on Computer Vision (ECCV)*, 2018, pp. 731–747.
- [4] T. Karras, S. Laine, M. Aittala, J. Hellsten, J. Lehtinen, and T. Aila, "Analyzing and Improving the Image Quality of Stylegan," in *Proceedings of the IEEE/CVF Conference on Computer Vision and Pattern Recognition*, 2020, pp. 8110–8119.
- [5] D. Ulyanov, A. Vedaldi, and V. S. Lempitsky, "Deep Image Prior," *2018 IEEE/CVF Conference on Computer Vision and Pattern Recognition*, pp. 9446–9454, 2018.
- [6] Z. Mao, N. Chimitt, and S. H. Chan, "Accelerating Atmospheric Turbulence Simulation Via Learned Phase-to-Space Transform," in *Proceedings of the IEEE/CVF International Conference on Computer Vision*, 2021, pp. 14759–14768.
- [7] —, "Image Reconstruction of Static and Dynamic Scenes Through Anisoplanatic Turbulence," *IEEE Transactions on Computational Imaging*, vol. 6, pp. 1415–1428, 2020.
- [8] D. L. Fried, "Probability of Getting a Lucky Short-Exposure Image Through Turbulence," *Journal of the Optical Society of America*, vol. 68, pp. 1651–1658, 1978.
- [9] N. M. Law, C. D. Mackay, and J. Baldwin, "Lucky Imaging: High Angular Resolution Imaging in the Visible From the Ground," *Astronomy & Astrophysics*, vol. 446, no. 2, p. 739–745, Jan 2006. [Online]. Available: <http://dx.doi.org/10.1051/0004-6361:20053695>
- [10] T. J. Schulz, "Multiframe Blind Deconvolution of Astronomical Images," *JOSA A*, vol. 10, no. 5, pp. 1064–1073, 1993.
- [11] F. Sroubek and P. Milanfar, "Robust Multichannel Blind Deconvolution via Fast Alternating Minimization," *IEEE Transactions on Image Processing*, vol. 21, no. 4, pp. 1687–1700, 2011.
- [12] K. Dabov, A. Foi, V. Katkovnik, and K. Egiazarian, "Image Denoising by Sparse 3-D Transform-Domain Collaborative Filtering," *IEEE Transactions on Image Processing*, vol. 16, no. 8, pp. 2080–2095, 2007.
- [13] R. Yasarla and V. M. Patel, "Learning to Restore a Single Face Image Degraded by Atmospheric Turbulence Using Cnns," *ArXiv Preprint ArXiv:2007.08404*, 2020. [Online]. Available: <https://arxiv.org/pdf/2007.08404>
- [14] —, "Learning to Restore Images Degraded by Atmospheric Turbulence Using Uncertainty," in *2021 IEEE International Conference on Image Processing (ICIP)*, IEEE. IEEE, 2021, pp. 1694–1698.
- [15] C. P. Lau, H. Souri, and R. Chellappa, "ATFaceGAN: Single Face Image Restoration and Recognition From Atmospheric Turbulence," *2020 15th IEEE International Conference on Automatic Face and Gesture Recognition (FG 2020)*, pp. 32–39, 2020.
- [16] P. Wieschollek, M. Hirsch, B. Scholkopf, and H. Lensch, "Learning Blind Motion Deblurring," in *Proceedings of the IEEE International Conference on Computer Vision*, 2017, pp. 231–240.
- [17] A. Bora, A. Jalal, E. Price, and A. G. Dimakis, "Compressed Sensing Using Generative Models," in *International Conference on Machine Learning*, PMLR. PMLR, 2017, pp. 537–546.
- [18] Y. Wu, M. Rosca, and T. Lillicrap, "Deep Compressed Sensing," in *International Conference on Machine Learning*, PMLR. PMLR, 2019, pp. 6850–6860.
- [19] F. Latorre, V. Cevher *et al.*, "Fast and Provable Admm for Learning With Generative Priors," *Advances in Neural Information Processing Systems*, vol. 32, pp. 12027–12039, 2019.
- [20] J. Whang, Q. Lei, and A. Dimakis, "Compressed Sensing With Invertible Generative Models and Dependent Noise," in *NeurIPS 2020 Workshop on Deep Learning and Inverse Problems*, 2020.
- [21] A. Jalal, L. Liu, A. G. Dimakis, and C. Caramanis, "Robust Compressed Sensing of Generative Models," *ArXiv Preprint ArXiv:2006.09461*, 2020. [Online]. Available: <https://arxiv.org/pdf/2006.09461>
- [22] G. Daras, J. Dean, A. Jalal, and A. G. Dimakis, "Intermediate Layer Optimization for Inverse Problems Using Deep Generative Models," *ArXiv Preprint ArXiv:2102.07364*, 2021. [Online]. Available: <https://arxiv.org/pdf/2102.07364>
- [23] P. Hand, O. Leong, and V. Voroninski, "Phase Retrieval Under a Generative Prior," *Advances in Neural Information Processing Systems*, 2018.
- [24] Z. Liu, S. Ghosh, and J. Scarlett, "Towards Sample-Optimal Compressive Phase Retrieval With Sparse and Generative Priors," *Advances in Neural Information Processing Systems*, vol. 34, 2021.
- [25] C. A. Metzler and G. Wetzstein, "Deep S<sup>3</sup>PR: Simultaneous Source Separation and Phase Retrieval Using Deep Generative Models," in *IEEE International Conference on Acoustics, Speech and Signal Processing*, IEEE. IEEE, 2021, pp. 1370–1374.
- [26] P. Hand and B. Joshi, "Global Guarantees for Blind Demodulation With Generative Priors," *Advances in Neural Information Processing Systems*, 2019.
- [27] D. Ren, K. Zhang, Q. Wang, Q. Hu, and W. Zuo, "Neural Blind Deconvolution Using Deep Priors," in *Proceedings of the IEEE/CVF Conference on Computer Vision and Pattern Recognition*, 2020, pp. 3341–3350.
- [28] M. Asim, F. Shamshad, and A. Ahmed, "Blind Image Deconvolution Using Deep Generative Priors," *IEEE Transactions on Computational Imaging*, vol. 6, pp. 1493–1506, 2020.
- [29] J. Liang, K. Zhang, S. Gu, L. Van Gool, and R. Timofte, "Flow-Based Kernel Prior With Application to Blind Super-Resolution," in *Proceedings of the IEEE/CVF Conference on Computer Vision and Pattern Recognition*, 2021, pp. 10601–10610.
- [30] J. W. Goodman, *Introduction to Fourier Optics*, 3rd ed. Englewood, Colo: Roberts & Co., 2005.
- [31] R. J. Noll, "Zernike Polynomials and Atmospheric Turbulence," *Journal of the Optical Society of America*, vol. 66, pp. 207–211, 1976.
- [32] N. Chimitt and S. H. Chan, "Simulating Anisoplanatic Turbulence by Sampling Correlated Zernike Coefficients," in *2020 IEEE International Conference on Computational Photography (ICCP)*, IEEE. IEEE, 2020, pp. 1–12.
- [33] I. Gulrajani, F. Ahmed, M. Arjovsky, V. Dumoulin, and A. C. Courville, "Improved Training of Wasserstein GANs," in *Advances in Neural Information Processing Systems*, ser. NeurIPS 2017, 2017.
- [34] D. P. Kingma and J. Ba, "Adam: a Method for Stochastic Optimization," *CoRR*, vol. abs/1412.6980, 2015.
- [35] A. Paszke *et al.*, "PyTorch: An Imperative Style, High-Performance Deep Learning Library," in *Advances in Neural Inf. Process. Systems*, vol. 32, 2019.
- [36] Z. Liu, P. Luo, X. Wang, and X. Tang, "Deep Learning Face Attributes in the Wild," in *Proceedings of International Conference on Computer Vision (ICCV)*, December 2015.
- [37] T. Karras, S. Laine, and T. Aila, "A Style-Based Generator Architecture for Generative Adversarial Networks," *2019 IEEE/CVF Conference on Computer Vision and Pattern Recognition (CVPR)*, pp. 4396–4405, 2019.
- [38] D. Roich, R. Mokady, A. H. Bermano, and D. Cohen-Or, "Pivotal Tuning for Latent-Based Editing of Real Images," *ArXiv Preprint ArXiv:2106.05744*, 2021.
- [39] O. Ronneberger, P. Fischer, and T. Brox, "U-Net: Convolutional Networks for Biomedical Image Segmentation," in *MICCAI*, 2015.